
Article:
Lu, Z. orcid.org/0000-0002-9967-5221, Ge, L., Wang, G. et al. (6 more authors) (2018) Lattice distortion effects on the frustrated spin-1 triangular-antiferromagnet A3NiNb2O9 (A=Ba, Sr, and Ca). Physical Review B, 98 (9). 094412. ISSN 2469-9950

https://doi.org/10.1103/physrevb.98.094412

Lattice distortion effects on the frustrated spin-1 triangular-antiferromagnet $A_3NiNb_2O_9$ (A = Ba, Sr, and Ca)

Z. Lu,[1] L. Ge,[2] G. Wang,[3] M. Russina,[1] G. Günther,[1] C. R. dela Cruz,[4] R. Sinclair,[5] H. D. Zhou,[5] and J. Ma[3,6,*]

[1]*Helmholtz-Zentrum Berlin für Materialien und Energie, D-14109 Berlin, Germany*

[2]*School of Physics, Georgia Institute of Technology, Atlanta, Georgia 30332, USA*

[3]*Key Laboratory of Artificial Structures and Quantum Control, School of Physics and Astronomy, Shanghai Jiao Tong University, Shanghai 200240, China*

[4]*Neutron Scattering Division, Oak Ridge National Laboratory, Oak Ridge, Tennessee 37831, USA*

[5]*Department of Physics and Astronomy, University of Tennessee, Knoxville, Tennessee 37996, USA*

[6]*Collaborative Innovation Center of Advanced Microstructures, Nanjing, Jiangsu 210093, China*

(Received 11 May 2018; published 11 September 2018)

In geometrically frustrated materials with low-dimensional and small spin moment, the quantum fluctuation can interfere with the complicated interplay of the spin, electron, lattice, and orbital interactions, and host exotic ground states such as the nematic spin state and chiral liquid phase. While the quantum phases of the one-dimensional chain and $S = \frac{1}{2}$ two-dimensional triangular-lattice antiferromagnet (TLAF) have been more thoroughly investigated by both theorists and experimentalists, the work on the $S = 1$ TLAF has been limited. We induced the lattice distortion into the TLAFs $A_3NiNb_2O_9$ (A = Ba, Sr, and Ca) with $S(Ni^{2+}) = 1$, and applied thermodynamic, magnetic, and neutron scattering measurements. Although $A_3NiNb_2O_9$ kept the noncollinear 120° antiferromagnetic phase as the ground state, the Ni^{2+} lattice changed from an equilateral triangle (A = Ba) into an isosceles triangle (A = Sr and Ca). The inelastic neutron scattering data were simulated by the linear spin-wave theory, and the competition between the single-ion anisotropy and the exchange anisotropy from the distorted lattice are discussed.

DOI: 10.1103/PhysRevB.98.094412

I. INTRODUCTION

In the geometrically frustrated system, the complicated interaction(s) between electron, phonon, spin, and orbital can lead to degenerate ground states, which introduce exotic properties and have attracted a lot of attention over the past decades [1–3]. Meanwhile, these degenerate states would easily be held by the symmetrical inconsistency and be destroyed by significant quantum fluctuations, not only induced by the complicated interactions among low dimensionality, geometrical frustration, small spin, and the applied magnetic field, but also modifying the classical Heisenberg model [4,5]. The triangular-lattice antiferromagnet (TLAF), one of the simplest frustrated two-dimensional (2D) materials, has been suggested to be strongly influenced by the strong quantum spin fluctuations with small effective spin ($S = \frac{1}{2}$ or 1) and exhibits a rich variety of interesting physics [6–8]. A striking example of these quantum phenomena is the transition from a noncollinear 120° spin configuration at 0 T into a fractional-magnet lattice under a finite range of applied magnetic field, such as a collinear up-up-down (*uud*) phase corresponding to a magnetization plateau with one-third of its saturation value [9–13].

Recently, theoretical research indicated the *uud* state as a commensurate analog of the incommensurate spin density wave which was predicted and observed for frustrated one-dimensional spin-1 chains and the $S = \frac{1}{2}$ TLAF [14,15], and suggested the possibility of exotic magnetic excitations. While there has been a great deal of theoretical activity in the domain, a full consensus on the origin of the *uud* state (even the ground magnetic state, noncollinear 120° at zero field) has been limited. This is true as well for the state-of-the-art experimental investigation of its spin excitations due to the lack of triangular-lattice materials. Although the lattice distortion has been believed to influence the quantum effects in the systems of kagome, square, and triangular motifs via the antisymmetric Dzyaloshinskii-Moriya (DM) interaction and requires that the dynamic models include the item of the lattice contribution [16–20], how the ground state of the triangular lattice originates from the lattice is still unclear. If the distortion effect were gradually introduced in the system, it would be insightful to obtain the specific physical properties as the related lattice is changed.

$Ba_3NiNb_2O_9$ was one of the first-studied equilateral TLAFs with highly symmetric crystal structure, which was free from the antisymmetric DM interaction such that a simple Hamiltonian model was expected to describe the physics of this material. The crystal structure is trigonal, P-3m1: (i) the corner oxygen is shared by the NiO_6 and NbO_6 octahedra; (ii) Ni ions occupy the 1b Wyckoff sites and form the triangular lattice in the ab plane; (iii) Ba^{2+} ions build up the unit cell frame and split NiO_6 octahedra. As the ab planes are separated by double nonmagnetic layers consisting of the Nb_2O_{11} double octahedra and Ba^{2+} ions, it is expected that the interlayer exchange interaction would be much smaller compared to the nearest-neighbor (NN) exchange interaction

*Corresponding author: jma3@sjtu.edu.cn

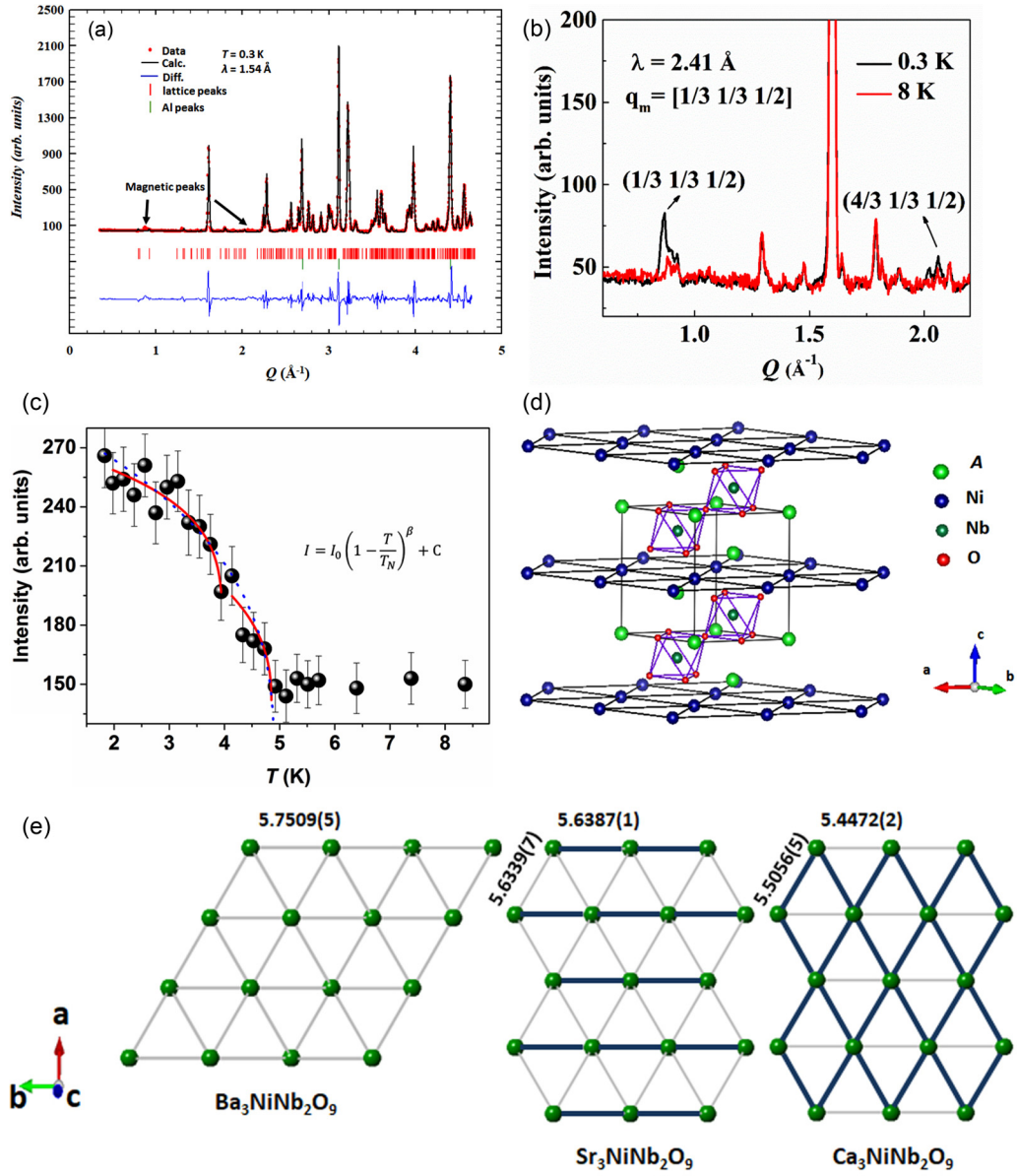

FIG. 1. (a) The neutron powder diffraction (NPD) pattern of polycrystalline $Ca_3NiNb_2O_9$ performed at 0.3 K. The refinement was done using the monoclinic space group, $P12_1/c1$. (b) The NPD patterns taken at 0.3 and 8 K. The (1/3, 1/3, 1/2) and (4/3, 1/3, 1/2) magnetic Bragg peaks at 0.3 K are given based on the hexagonal P-$3m1$ space group. (c) Temperature dependence of the order parameter in $Ca_3NiNb_2O_9$. Lines are fits to one (dashed) or two (solid) order parameters. The latter fit the data better suggesting a two-step transition consistent with what is observed in the bulk magnetization measurements discussed in the next section. (d) The schematic crystal structure of $A_3NiNb_2O_9$. (e) Triangle lattice of Ni^{2+} ions in ab plane of $A_3NiNb_2O_9$.

in the ab plane of Ni^{2+} ions and the compound could be treated or approximately treated as a 2D system.

In this paper, we focus on the ground state of the non-collinear 120° spin structure reported for the triangular-lattice antiferromagnets $A_3NiNb_2O_9$ (A = Ba, Sr, and Ca). Since the magnetic exchange energies are sensitive to the bond lengths/angles of Ni and O ions, it is interesting to compare the family of $A_3NiNb_2O_9$ (A = Ba, Sr, and Ca) as the structures are gradually distorted. As Sr^{2+} and Ca^{2+} ions are smaller than the Ba^{2+} ion, the effect from the lattice distortion is introduced gradually and the A-site effect on the exchange interactions is observed. In addition, a strong coupling between the successive magnetic phase transitions and the ferroelectricity has been observed in $Ba_3NiNb_2O_9$ and $Sr_3NiNb_2O_9$ by magnetic and electric bulk measurements [10,21]. Our study on the lattice effect on the triangular lattice should not only discuss the quantum effect in TLAFs, but also be beneficial for the development of multiferroicity theory in low-dimensional frustrated materials [22].

II. EXPERIMENTAL

Polycrystalline $A_3NiNb_2O_9$ (A = Ba, Sr, and Ca) samples were prepared with the solid state reaction method. Stoichiometric mixtures of $BaCO_3$/$SrCO_3$/$CaCO_3$, NiO, and Nb_2O_5 were ground together, and calcined in air at 1230 °C for

24 h. A commercial SQUID magnetometer (MPMS, Quantum Design) and a high-field vibrating sample magnetometer (VSM) were employed to measure the dc magnetization as a function of temperature and magnetic field. The specific heat was measured with a physical property measurement system (PPMS, Quantum Design) in two steps. First, the background specific heat was measured by an empty pucker with *N*-grease; then, a dense and solid thin plate of the $A_3NiNb_2O_9$ sample with a total mass around 10 mg was measured. After that, by subtracting the background specific heat from this total specific heat, we obtained the specific heat of the sample.

The neutron powder diffraction (NPD) measurements down to 0.3 K were performed using the HB-2A powder diffractometer at the High Flux Isotope Reactor (HFIR), Oak Ridge National Laboratory (ORNL), with a ^{3}He insert system. About 5 g of pelletized powder for each sample was loaded in a vanadium can with He exchange gas. Data were collected at selected temperatures using two different wavelengths $\lambda = 1.538$ and 2.406 Å. The collimation was set as open-open-6′. The shorter wavelength was used to investigate the crystal structures with the higher Q coverage, while the longer wavelength was important for investigating the magnetic structures of the material with the lower Q coverage. The Rietveld refinements on the diffraction data were performed using the program FullProf [23].

The inelastic neutron scattering (INS) of polycrystalline $A_3NiNb_2O_9$ (A = Ba, Sr, and Ca) samples was carried out on the recently upgraded cold-neutron direct-geometry time-of-flight spectrometer NEAT at Helmholtz-Zentrum Berlin [24]. The spectrometer allows us to cover a wide range of energy transfers $\hbar\omega$ and scattering angles, thereby allowing determination of a large swath of the scattering intensity $S(Q, \omega)$ as a function of momentum transfer $\hbar Q$ and energy transfer $\hbar\omega$, where Q is the scattering vector. Around 4 g of each sample was packed in aluminum cans filled with He exchange gas. Each scan was counted around 6 hours with the incident neutron energy $E_i = 3.272$ meV.

III. RESULTS

A. Neutron powder diffraction

As shown in Figs. 1(a) and 1(b), low-temperature NPD was employed at 8 and 0.3 K to identify the magnetic structure of polycrystalline $Ca_3NiNb_2O_9$. The space group could be indexed using a monoclinic unit cell, space group $P12_1/c1$ (No. 14), with one Ni atom at the 2a (0, 0, 0) site and another one at the 2d site (1/2, 1/2, 1/2), and the other Ca, Nb, and O atoms at the 8f (x, y, z) site. By comparing the Rietveld refinement results of $Ca_3NiNb_2O_9$ patterns at 0.3 and 20 K (20 K data are not presented here), it is suggested that no crystal structure ($P12_1/c1$) transition was observed down to 0.3 K. The (1/3, 1/3, 1/2) and (4/3, 1/3, 1/2) magnetic Bragg peaks were observed at 0.3 K and absent at 8 K with $Q \sim 0.85$ Å^{-1} and 2.0 Å^{-1}, which is consistent with the commensurate magnetic wave vector $\mathbf{q_m} = [1/3, 1/3, 1/2]$ [Fig. 1(b)], suggesting a similar 120° spin structure to $Ba_3NiNb_2O_9$ and $Sr_3NiNb_2O_9$ at 0.3 K [10,21]. The magnetic phase transition was displayed by the temperature dependence of the order parameter (OP), Fig. 1(c), measured as the temperature dependence of the intensity of the [1/3, 1/3, 1/2] magnetic peak.

Figure 1(d) presents the schematic crystal structure of $A_3NiNb_2O_9$. For the triple-perovskite system $A_3NiNb_2O_9$, the Ni-triangular layers were split by the nonmagnetic corner-shared Nb_2O_{11} perovskite. At the substitution of the smaller ions into the Ba site with Ca^{2+}, the lattice of $Ca_3NiNb_2O_9$ was distorted from the hexagonal (P-32/m1) to monoclinic ($P12_1/c1$) space group as $Sr_3NiNb_2O_9$. Therefore, the equilateral Ni triangle changed to an isosceles triangle by replacing the Ba^{2+} ions with Sr^{2+} and Ca^{2+} ions, Fig. 1(e). The Ba compound exhibited an equilateral Ni triangle with bonds of 5.7509 Å. For the Sr compound, one longer bond of 5.6387 Å and two shorter bonds of 5.6339 Å were obtained; for the Ca compound, one shorter bond of 5.4470 Å and two longer bonds of 5.5056 Å were observed.

The tolerance factor, t, suggested by Goldschmidt has been employed to describe the stability of perovskite phases: the deviation of t from $t = 1$ can be applied to estimate the internal strain in perovskites and oxygen octahedral tilt due to the misfit of the A and B site ionic radii [25]. The definition of t is given by

$$t = \frac{R_A + R_O}{\sqrt{2}(\langle R_B \rangle + R_O)},$$

where $\langle R_B \rangle$ is the average ionic radii for the B-site ions [26], and R_A and R_O are the A- and O-site ionic radii, respectively.

The crystallographic properties of $A_3NiNb_2O_9$ (A = Ba, Sr, and Ca) are given in Table I. For $Ba_3NiNb_2O_9$, the tolerance factor is bigger than 1 while it is smaller than 1 for $Sr_3NiNb_2O_9$. However, the t deviations from $t = 1$ are similar with ~0.030, which suggests a similar distortion from the ideal perovskite for them. Therefore, the crystal structure

TABLE I. Crystallographic properties of $A_3NiNb_2O_9$ (A = Ba, Sr, and Ca).

Parameters	$Ba_3NiNb_2O_9$ [10]	$Sr_3NiNb_2O_9$ [21]	$Ca_3NiNb_2O_9$
Space group	P-32/m1	$P12_1/c1$	$P12_1/c1$
Lattice parameters	$a = b = 5.7509(5)$ Å $c = 7.0343(8)$ Å	$a = 9.7549(5)$ Å $b = 5.6387(1)$ Å $c = 16.9194(8)$ Å	$a = 9.5695(8)$ Å $b = 5.4472(2)$ Å $c = 16.7876(3)$ Å
Interaxial angles	$\alpha = \beta = 90°$ $\gamma = 120°$	$\alpha = \gamma = 90°$ $\beta = 125.066(4)°$	$\alpha = \gamma = 90°$ $\beta = 125.718(3)°$
t	1.031	0.972	0.938

TABLE II. Bond lengths of $A_3NiNb_2O_9$ (A = Ba, Sr, and Ca).

Bonds	$Ba_3NiNb_2O_9$ [10]	$Sr_3NiNb_2O_9$ [21]	$Ca_3NiNb_2O_9$
$\langle Ba_1/Sr_1/Ca_1\text{-O}\rangle$	2.8695(1)	2.7829(4)	2.7345(3)
$\langle Ba_2/Sr_2/Ca_2\text{-O}\rangle$	2.8850(9)	2.8243(4)	2.8689(2)
$\langle Sr_3/Ca_3\text{-O}\rangle$	–	2.8962(6)	2.8560(9)
$\langle Ni_1\text{-O}\rangle$	2.0901(3)	1.9416(9)	2.1165(9)
$\langle Ni_2\text{-O}\rangle$	–	2.0449(5)	2.0653(4)
$\langle$Ni-O$\rangle$	–	1.9933(2)	2.0909(6)
$\langle Nb_1\text{-O}\rangle$	1.9416(7)	2.0004(7)	2.0005(5)
$\langle Nb_2\text{-O}\rangle$	2.0662(2)	2.0731(1)	2.0625(8)
$\langle$Nb-O$\rangle$	2.0039(5)	2.0367(9)	2.0315(6)

distorted from hexagonal to monoclinic structure is expected to result in a smaller t. Moreover, the angles of the equilateral triangle in $Ba_3NiNb_2O_9$ are all 60°; for $Sr_3NiNb_2O_9$, they are 60.090°, 59.955°, and 59.955°; and for $Ca_3NiNb_2O_9$, they are 58.930°, 60.535°, and 60.535°.

Table II shows the bond lengths of $A_3NiNb_2O_9$ (A = Ba, Sr, and Ca). Considering the bond length, the six Ni-O bonds had the same lengths of 2.090 Å in $Ba_3NiNb_2O_9$. However, the smaller ionic radius of Nb^{5+}, 0.64 Å, compared to 0.69 Å for Ni^{2+} in octahedral coordination resulted in breathing distortion (extension or contraction of the Nb-O bond lengths) of the NbO_6 octahedra with two different lengths of Nb-O bonds, 1.942 and 2.066 Å, respectively. In $Sr_3NiNb_2O_9$ and $Ca_3NiNb_2O_9$, the A-site ion is too small to hold its occupied cuboctahedral site, and then a combination of the breathing and tilting distortions both occurred, which can reduce the volume of the interstice and thereby improve the structural stability. With decreasing the size of the A-site ion, for $Sr_3NiNb_2O_9$ the average bond lengths of A-O and B-O decreased, but for $Ca_3NiNb_2O_9$ the smallest A-site ion the $\langle A\text{-O}\rangle$ and $\langle B\text{-O}\rangle$ are bigger than those for $Sr_3NiNb_2O_9$ due to stronger lattice distortion.

In Fig. 1(c), the fitting of OP was assumed with one or two order parameters, shown as dashed and solid lines, respectively. $T_{N1} = 4.90$ K was obtained with the single-OP fitting with $\beta_{one} \approx 0.39$. The two-OP fitting gave $T_{N1} = 4.85$ K and $T_{N2} = 4.05$ K and yielded critical exponents $\beta_{two\text{-}1} \approx 0.34$ and $\beta_{two\text{-}2} \approx 0.36$, respectively, which were a better description of the data. It is worth noting that the obtained values are comparable with those of 2-vector XY ($\beta = 0.35$) or 3-vector Heisenberg ($\beta = 0.36$) models. The latter fit the data better suggesting a two-step transition consistent with what is observed in the bulk magnetization measurements discussed in the next section. However, the effect of averaging in powder diffraction and the limited Q range of the instruments can only determine the 120° spin direction projected in the ab plane and cannot determine whether the systems form a coplanar magnetic structure or not [27]; more details can be analyzed by the dynamics.

B. Magnetic susceptibility and heat capacity

Figure 2(a) shows the specific heat data of the $Ca_3NiNb_2O_9$ at different fields. A peak was observed around 4.2 K in the zero-field curve. According to the literature on $Sr_3NiNb_2O_9$ [21] and $Ba_3NiNb_2O_9$ [10], this peak corresponds to the long-range magnetic order transition. As the magnetic field increases, the peaks shift to lower temperature and become broader. In Fig. 2(b), C_p/T vs T and dC_p/dT vs T present two anomalies as T_{N2} and T_{N1}, respectively, which are similar to $Sr_3NiNb_2O_9$ and should be related to the distorted lattice.

The temperature dependence of the dc susceptibility of $Ca_3NiNb_2O_9$ with different magnetic fields is shown in Fig. 3(a). As the field increases, the magnetic transition temperatures decrease and become broader similarly to the behavior of the heat capacity anomaly. The data at 0.02 T follow the Curie-Weiss law at high temperature (inset). Fitting the $\chi(T)$ data from 100–300 K with a linear Curie-Weiss law,

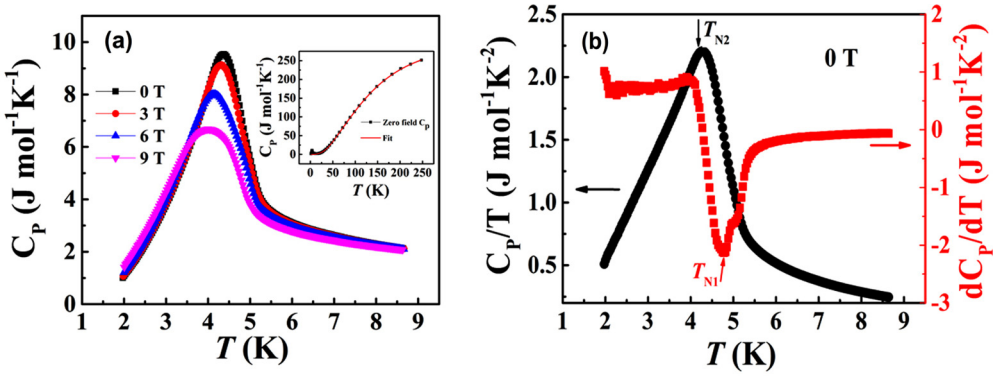

FIG. 2. (a) Temperature dependence of the specific heat for the polycrystalline $Ca_3NiNb_2O_9$ sample at different magnetic fields. The inset is the specific heat at zero field and fit. (b) Temperature dependence of C_p/T and dC_p/dT around T_{N1} and T_{N2} at zero magnetic field.

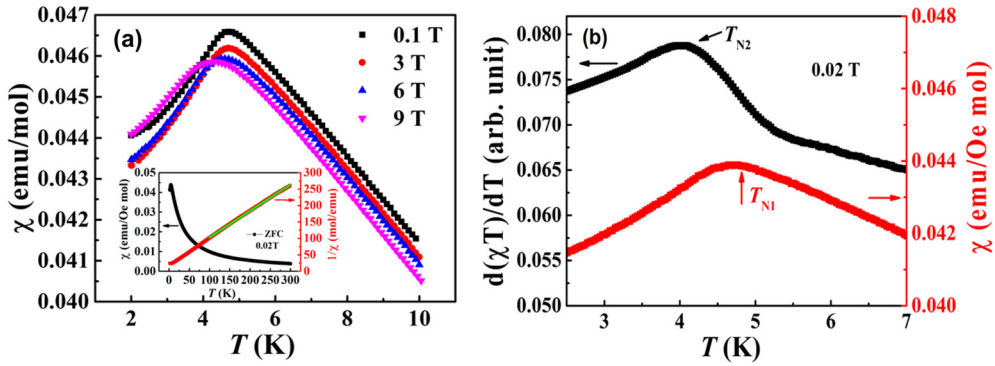

FIG. 3. (a) Temperature dependence of susceptibility around the phase transition at different fields. The inset is temperature dependence of χ and $1/\chi$ for the polycrystalline $Ca_3NiNb_2O_9$ sample at $H = 0.02$ T. The green line is the linear fit of $1/\chi$ from 100 K to 300 K. (b) The temperature dependence of $d(\chi T)/dT$ and χ from 2.5 to 7 K.

we obtain −28 K for the Curie-Weiss temperature (θ_{CW}) suggesting the dominance of antiferromagnetic (AFM) exchange interactions. For $Ca_3NiNb_2O_9$, $S = 1$, the effective moment (μ_{eff}) is calculated as 3.16 μ_B/Ni with a corresponding Landé g factor of 2.23, based on $\mu_{eff} = g\sqrt{S(S+1)}\mu_B$, which is comparable with those of $Ba_3NiNb_2O_9$, $Sr_3NiNb_2O_9$, and other compounds with Ni^{2+} ions [9,10,21,28,29].

The spin frustration ratio f is defined as the ratio of the absolute value of the Curie-Weiss temperature (θ_{CW}) to transition temperature T_N; thus $f = |\theta_{CW}|/T_N$. For $Sr_3NiNb_2O_9$ and $Ca_3NiNb_2O_9$ samples, we chose the higher transition temperature, T_{N1}, for calculation. As shown in Table III, the frustration ratio f increases with decreasing the A-site ion radii, and $Ca_3NiNb_2O_9$ has the strongest frustration and competing interactions.

From Fig. 3(b), the χ data exhibit a clear peak at ∼4.8 K, which is consistent with T_{N1} from the dC_p/dT data. Another peak can be observed from the $d(\chi T)/dT$ at ∼4.2 K, which is related to a long-range magnetic ordering and corresponds to T_{N2} defined from the specific heat, Fig. 2(b). It is worth noting for the Ca compound that the two-step phase transition is not so strong and sensitive to different measurement techniques to some extent. For example, the T_{N2} transition is more sensitive to thermal measurement while the T_{N1} transition can be detected more easily by dc susceptibility. Figure 4(a) compares the temperature dependence of C_p/T for the polycrystalline $A_3NiNb_2O_9$ (A = Ba, Sr, and Ca) samples at zero magnetic field. The Ba compound exhibits the sharpest peak with the lambda-type feature in specific heat data, which results from its single-step phase transition at zero field. As shown in Fig. 4(b), at low magnetic fields, the temperature dependence of $d(\chi T)/dT$ for the polycrystalline $Ba_3NiNb_2O_9$ sample also shows a sharp peak at T_N, while the two nearby T_N peaks of the Sr and Ca compounds indicate a two-step transition for them.

TABLE III. Parameters extracted from the specific heat and dc susceptibility measurements for $A_3NiNb_2O_9$ (A = Ba, Sr, and Ca).

Parameters	$Ba_3NiNb_2O_9$ [10]	$Sr_3NiNb_2O_9$ [21]	$Ca_3NiNb_2O_9$
T_{N1} (K)	4.9	5.5	4.8
T_{N2} (K)	–	5.1	4.2
θ_{CW} (K)	−16.4	−21.5	−28
μ_{eff} (μ_B/Ni)	3.15	3.21	3.16
g	2.23	2.27	2.23
f	3.4	3.9	5.83

Based on the mean-field theory, the Heisenberg Hamiltonian, $J\sum_{\langle i,\ j\rangle}(S_iS_j)$, can be approximately related to the exchange J and the Curie-Weiss temperature θ_{CW}, $J = -3k_B\theta_{CW}/zS(S+1)$. For $A_3NiNb_2O_9$ (A = Ba, Sr, and Ca), each Ni^{2+} ion is surrounded by 6 NNs ($z = 6$) with the interaction J in the triangular lattice; hence, $J/k_B = -3\theta_{CW}/12$, and J_{Ba}/k_B, J_{Sr}/k_B, and J_{Ca}/k_B are ∼4.1 K (0.35 meV), 5.4 K (0.46 meV), and 7.0 K (0.60 meV), respectively. Therefore, the Sr and Ca compounds exhibit larger J than the Ba compound according to the calculated results.

The magnetic entropy of the $A_3NiNb_2O_9$ is shown in the inset of Fig. 4(a). The total magnetic entropy suggests that the degree of disorder of these three compounds is Ca > Sr > Ba, which is consistent with the behavior of the tolerance factor t in Table I. To extract the magnetic contribution from the total heat capacity, an equation consisting of the linear combination of one Debye and several Einstein terms is used to estimate the lattice specific heat,

$$C_L(T) = C_D\left[9R\left(\frac{T}{\theta_D}\right)^3\int_0^{\theta_D/T}\frac{x^4e^x}{(e^x-1)^2}dx\right] + \sum_i C_{E_i}\left[3R\left(\frac{\theta_{E_i}}{T}\right)^2\frac{\exp\left(\frac{\theta_{E_i}}{T}\right)}{\left[\exp\left(\frac{\theta_{E_i}}{T}\right)-1\right]^2}\right],$$

where R is the universal gas constant, and θ_D, θ_E are the Debye and Einstein temperatures, respectively. C_D, C_{E_i} are the relative weights of the acoustic and the optical phonon contribution of the heat capacity. There are 15 atoms per formula in our system. The best fit to the data from 30 to 250 K result in one Debye and two Einstein terms with the proportion 1 : 5 : 9 for the $C_D : C_{E_1} : C_{E_2}$, and $\theta_D = 160$ K, $\theta_{E_1} = 255$ K, $\theta_{E_2} = 540$ K. The magnetic component of the specific heat C_m is obtained after subtracting the lattice contribution from the data. The magnetic entropy S_m is obtained by integrating C_mT throughout the range of temperatures measured [inset of Fig. 4(a)]. The Ni^{2+} has a spin-1 in this compound. The total entropy saturated at about 79.1% of the Rln3. The entropy

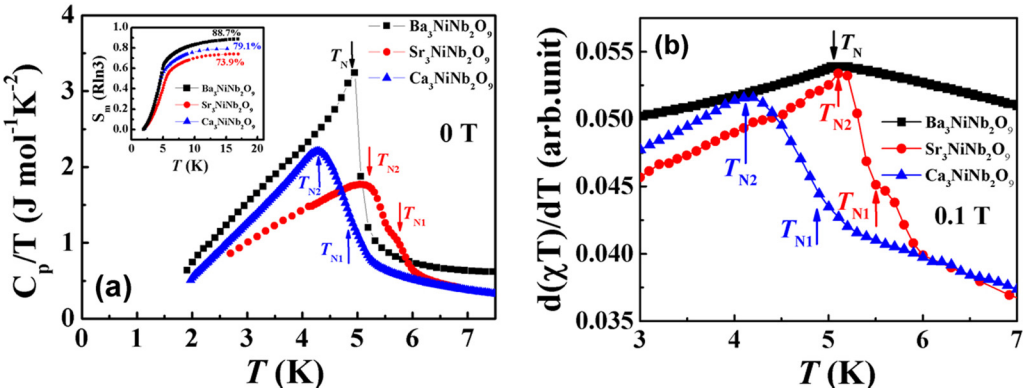

FIG. 4. (a) The comparison of the specific heat for $A_3NiNb_2O_9$ at zero magnetic field. The inset is the magnetic entropy of $A_3NiNb_2O_9$. (b) The comparison of the $d(\chi T)/dT$ for $A_3NiNb_2O_9$ at very low magnetic fields.

loss could be due to the quantum fluctuation in this spin frustrated system. We also measured the heat capacity of the $Sr_3NiNb_2O_9$ and $Ba_3NiNb_2O_9$, and then processed the data with the same method of $Ca_3NiNb_2O_9$. The total magnetic entropy was about 73.9% and 88.7% of $R\ln 3$ for $Sr_3NiNb_2O_9$ and $Ba_3NiNb_2O_9$, respectively. The total magnetic entropy decreased as Ba > Ca > Sr, which indicated the smallest magnetic entropy loss of Ba compound due to its smallest lattice distortion. However, for the Sr and Ca compounds, the magnetic entropy losses were dominated by the competition effect between lattice distortion and quantum fluctuation.

C. Inelastic neutron scattering

To explore the spin dynamics of $A_3NiNb_2O_9$ (A = Ba, Sr, and Ca) in detail, we measured the magnetic excitations from INS spectra. Figures 5(a)–5(c) show the powder spectrum of $A_3NiNb_2O_9$ (A = Ba, Sr, and Ca) at 1.5 K, below T_N. Similarly to the $S = \frac{1}{2}$ TLAF compound, $Ba_3CoSb_2O_9$, both gapped and gapless modes are observed in the magnetic DOS [27]; meanwhile, unlike $Ba_3CoSb_2O_9$, there is no obvious continuum observed at higher energy, which might be due to the larger spin moment ($S = 1$) and the weak signal from the powder average effect.

The low-energy magnon bandwidth of $Ba_3NiNb_2O_9$ is around 1.0 meV, which is lower than those of $Sr_3NiNb_2O_9$ and $Ca_3NiNb_2O_9$ (~1.25 meV). The magnetic DOS of the $A_3NiNb_2O_9$ (A = Ba, Sr, and Ca) system showed minima around $Q \approx 0.85$ Å^{-1}, which notably corresponds to commensurate magnetic wave vector $\mathbf{q_m} = [1/3, 1/3, 1/2]$. Moreover, the gaps of this branch at $\mathbf{q_m} = [1/3, 1/3, 1/2]$ for $Ba_3NiNb_2O_9$ and $Ca_3NiNb_2O_9$ were around 0.6 meV, while $Sr_3NiNb_2O_9$ exhibited a similar gap of around 0.8 meV, Figs. 5(a)–5(c). The magnetic signals were momentum-dependent due to stronger ridges of intensity at $Q \approx 0.85$ Å^{-1} than at $Q \approx 1.5$ Å^{-1} and $Q \approx 2.0$ Å^{-1}.

The INS results are simulated by the linear spin wave (LSW) theory based on the quasi-2D XXZ Hamiltonian on a vertically stacked triangular lattice, Figs. 5(d)–5(f). The appropriate Heisenberg Hamiltonian is

$$H = J \sum_{\langle i,\ j\rangle}^{\text{layer}} \left(S_i^x S_j^x + S_i^y S_j^y + \Delta S_i^z S_j^z\right) + J' \sum_{\langle l,\ m\rangle}^{\text{interlayer}} \mathrm{S}_l \cdot \mathrm{S}_m,$$

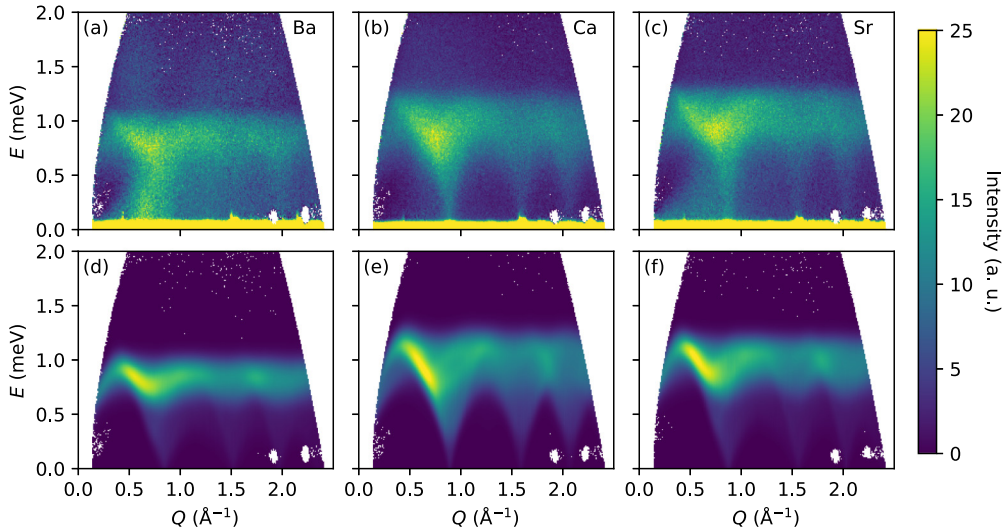

FIG. 5. Powder spectra measured experimentally at 1.5 K on spectrometer NEAT: (a) $Ba_3NiNb_2O_9$, (b) $Ca_3NiNb_2O_9$, (c) $Sr_3NiNb_2O_9$ powder spectra at 1.5 K. The powder-average LSW approximation of (d) $Ba_3NiNb_2O_9$, (e) $Ca_3NiNb_2O_9$, (f) $Sr_3NiNb_2O_9$.

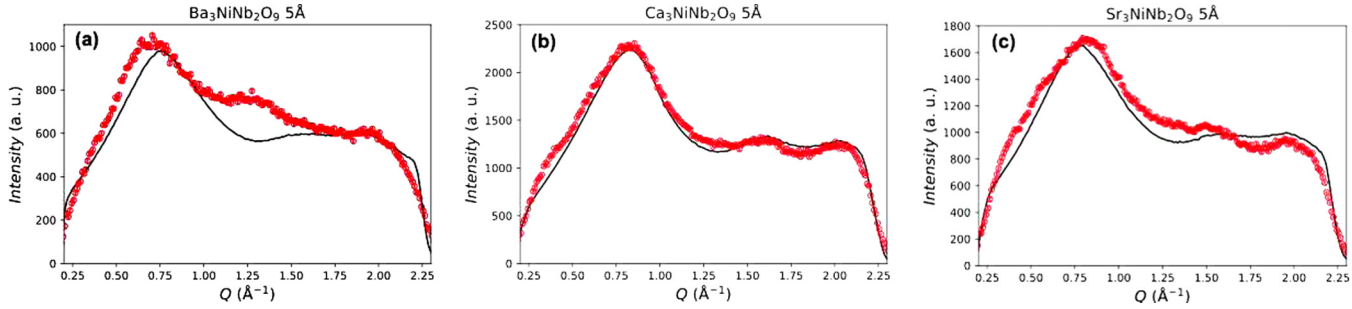

FIG. 6. Comparison between experiment (red dots) and LSWT (the black line) simulation shown as energy-integrated within $0.2 \leqslant E \leqslant 1.5$ meV for (a) $Ba_3NiNb_2O_9$, (b) $Ca_3NiNb_2O_9$, (c) $Sr_3NiNb_2O_9$.

where J and J' ($J, J' > 0$) are the intra- and interlayer NN antiferromagnetic exchange energies, respectively. Δ ($0 < \Delta \leqslant 1$) is the easy-plane exchange anisotropy from the same 120° structure as in the Heisenberg case. Although due to the isosceles triangular geometry in the Sr and Ca compounds, it is more intuitive to use two different exchanges for the intralayer coupling; the [1/3, 1/3, 1/2] wave vector requires them to be the same [30]. Table IV is a summary of the parameters in the Hamiltonian according to the LSW approximation.

The E-integrated scans are obtained in Fig. 6; INS measurements and the powder-averaged LSW approximation have a good agreement: the data of the Ca compound can be explained as the most Heisenberg-like feature, and the best fit is obtained.

In the $A_3NiNb_2O_9$ system, the Sr compound exhibits the largest intralayer NN exchange ($J = 0.36$ meV), while the Ca compound obtains the largest interlayer exchange ($J' = 0.3J$). Hence, the intra- and interlayer NN exchange satisfies these relations, $J_{Ba} < J_{Ca} < J_{Sr}$ and $J'_{Ba} < J'_{Sr} < J'_{Ca}$, respectively. And the mean-field theory does not work for $Sr_3NiNb_2O_9$ and $Ca_3NiNb_2O_9$, as shown in Table IV. The biggest gap for the Sr compound (~0.8 meV) suggests a larger intraplane NN exchange anisotropy than those of ~0.6 meV for the Ba and Ca compounds. When the Ba^{2+} ion is substituted with the smaller Sr^{2+} ion, the Ni^{2+} triangle changes from an equilateral triangle to an isosceles triangle, as shown in Fig. 1(e). The smaller A-site ions result in a smaller triangle lattice and larger intraplane exchange anisotropy. When the smallest Ca^{2+} ion is on the A site, the lattice distortion is enhanced further, and the interplane interaction was strong enough to affect the intraplane anisotropy, which presents the weak quantum effect. From the NPD data, the distances between the triangular ab planes for the Ba, Sr, and Ca compounds are 7.034 Å, 6.924 Å, and 6.815 Å, respectively.

TABLE IV. Summary of the exchange parameters in the Hamiltonian according to the LSW approximation.

Parameters	$Ba_3NiNb_2O_9$	$Ca_3NiNb_2O_9$	$Sr_3NiNb_2O_9$
J^{MFT} (meV)	0.35	0.60	0.46
J (meV)	0.30(1)	0.31(1)	0.36(1)
J'/J	0.05(5)	0.30(5)	0.05(5)
Δ	0.70(5)	0.95(5)	0.75(5)

And the ratios of the average intraplane Ni-Ni bond lengths to these interlayer distances are ~0.81 for the Ba and Sr compounds, and ~0.80 for the Ca one. Therefore, the shortest interlayer distances and the smallest ratios of bond lengths to plane distances for the Ca compound lead to very strong interplane coupling with the largest $J'/J = 0.30$ and reduce the J slightly to 0.31 meV ($< J_{Sr} = 0.36$ meV). In addition, the Ca compound shows a more obvious gapless feature than the Sr compound from the fitting. The best-fitting parameters of easy-plane exchange anisotropy are $\Delta = 0.95$ and $\Delta = 0.75$ for $Ca_3NiNb_2O_9$ and $Sr_3NiNb_2O_9$, respectively, as shown in Table IV. This indicates that the Ca compound has less easy-plane anisotropy compared to the Sr one due to its more dispersive feature with a similar bandwidth to the Sr compound.

The competition of the easy-plane exchange anisotropy Δ and J'/J is treated as the dominant effect in the $A_3NiNb_2O_9$ system. Moreover, we also consider the easy-axis anisotropy, single-ion anisotropy, and DM effects in the system by the LSW approximation: (1) Easy-axis anisotropy can lift the entire band up, create a gap, and modify the ordering wave vector. (2) If single-ion anisotropy exists, the out-of-plane canting would be bigger and towards the collinear structure. (3) DM interactions that stabilize the [1/3, 1/3, 1/2] structure have to be perpendicular to the easy plane and not overwhelmingly large. Within the LSW approximation, such DM terms would have very similar impact on the excitations and therefore are not considered here for simplicity. Since the Hamiltonian still has continuous symmetry in the easy plane, and the ground state can break it spontaneously, no matter how weak the powder spectra are, they will always be gapless.

IV. DISCUSSION

To understand the intralayer antiferromagnetic interaction of the Ni^{2+} ions, we examined the superexchange interaction in the structure using the Goodenough-Kanamori theoretical framework [31], which discusses the relation between the symmetry of electron orbitals and superexchange interaction via a nonmagnetic anion. In $Ba_3NiNb_2O_9$, two superexchange pathways for the Ni^{2+} spins in the same layer are shown in Fig. 7(a), Ni^{2+}-O^{2-}-O^{2-}-Ni^{2+} and Ni^{2+}-O^{2-}-Nb^{5+}-O^{2-}-Ni^{2+}, respectively, by sharing the corner oxygens of the NiO_6 and NbO_6 octahedrons. Although the first Ni^{2+}-O^{2-}-O^{2-}-Ni^{2+} superexchange pathway could

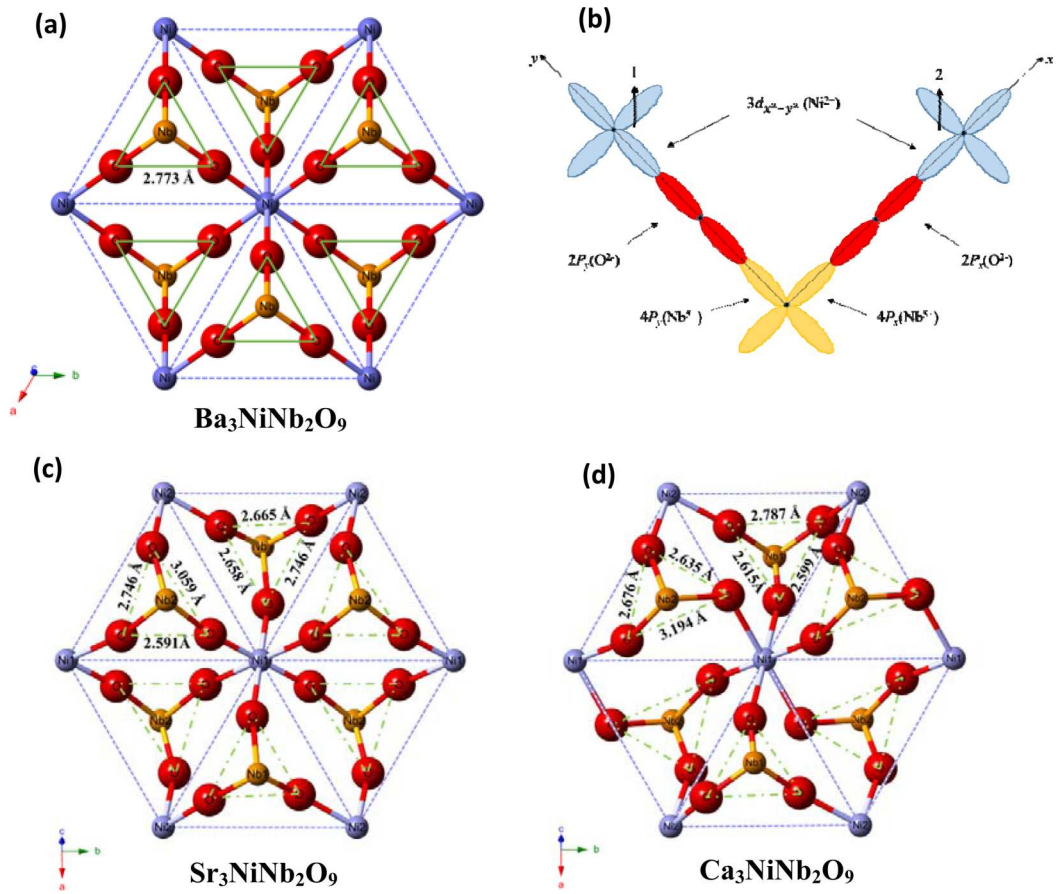

FIG. 7. (a) Superexchange pathways for FM Ni^{2+}-O^{2-}-O^{2-}-Ni^{2+} and AFM Ni^{2+}-O^{2-}-Nb^{5+}-O^{2-}-Ni^{2+} interactions in $Ba_3NiNb_2O_9$. (b) Orbital configurations of FM interactions through Ni^{2+}-O^{2-}-Nb^{5+}-O^{2-}-Ni^{2+} superexchange pathway in $Ba_3NiNb_2O_9$. (c) Superexchange pathways in $Sr_3NiNb_2O_9$. (d) Superexchange pathways in $Ca_3NiNb_2O_9$.

be observed as the antiferromagnet, the connection of O^{2-}-O^{2-} needs to hybridize/distort the s orbital or the other p orbitals of O^{2-}. For the second superexchange path of Ni^{2+}-O^{2-}-Nb^{5+}-O^{2-}-Ni^{2+}, Fig. 7(b), the superexchange interaction between the spins on the $d_{x^2-y^2}$ orbitals of the Ni^{2+} ions are considered. From the Rietveld refinements of neutron powder diffraction, the O^{2-}-Nb^{5+}-O^{2-} bond angle is very close to 90° at 91.13°, and the Ni^{2+}-O^{2-}-Nb^{5+} is 180°. In this case, the spin-1 on the left Ni^{2+} ion transferred to the $2p_y$ orbital of the O^{2-} by combining with the $2p_y$ orbital of the filled outermost Nb^{5+} $4p$ orbitals to form a molecular orbital while the spin-2 on the right Ni^{2+} ion transferred to the molecular orbital composed of the $2p_x$ orbital of the O^{2-} and the Nb^{5+} ions. According to Hund's rule, these two spins on the p_y and p_x orbitals must be parallel. Thus, a ferromagnetic superexchange interaction formed between these two Ni^{2+} ions after these two spins transferred back to the $d_{x^2-y^2}$ orbitals of Ni^{2+}. Therefore, the Ni^{2+}-O^{2-}-O^{2-}-Ni^{2+} exchange had a shorter connection path and thereby a stronger orbital distortion than the one of Ni^{2+}-O^{2-}-Nb^{5+}-O^{2-}-Ni^{2+}. For $Ba_3NiNb_2O_9$, the distortion effect was not dominant, and the AFM interaction overcame the FM interaction. As the magnetic field was applied, the distortion effect was strengthened, and the FM interaction could be observed in the *uud* phase [10]. Similar competitive superexchange interactions in other triangular-lattice models with layered perovskite structures have been reported. For example, in $Ba_3CoNb_2O_9$, the AFM Co^{2+}-O^{2-}-O^{2-}-Co^{2+} interaction is stronger than the FM Co^{2+}-O^{2-}-Nb^{5+}-O^{2-}-Co^{2+} interaction, which resulted in a weak AFM interaction [32]. However, in other triangular-magnet systems, such as $AAg_2M(VO_4)_2$ (A = Ba, Sr; M = Co, Ni) [33], the AFM Co^{2+}-O^{2-}-O^{2-}-Co^{2+} interaction was weaker than the FM Co^{2+}-O^{2-}-V^{5+}-O^{2-}-Co^{2+} interaction, and for $YCr(BO_3)_2$, the AFM Cr^{3+}-O^{2-}-O^{2-}-Cr^{3+} interaction was also weaker than the FM Cr^{3+}-O^{2-}-Yb^{3+}-O^{2-}-Cr^{3+} interaction [34].

As shown in Figs. 7(c) and 7(d), in $Sr_3NiNb_2O_9$ and $Ca_3NiNb_2O_9$, the lattice distortion results in the variation of the Ni^{2+}-O^{2-} bond lengths. Most of the O^{2-}-Nb^{5+}-O^{2-} bond angles are distorted away from the ideal value of 90°, to as small as ∼76° and some as large as ∼104°. The Ni^{2+}, O^{2-}, and Nb^{5+} ions are not on the same line. Thus, the FM interactions are influenced by the distortion and lead to stronger resultant AFM interactions. To obtain the *uud* phase, a higher magnetic field needs to be applied [21]. Meanwhile, the polarization of Sr and Ca compounds should be smaller than that of the Ba compound, and the reentrant

signal in pyroelectric current of the Ba compound is absent [21].

Moreover, only one transition is observed in $Ba_3NiNb_2O_9$, which is consistent with the easy-plane anisotropy in this isotropic system. For $Sr_3NiNb_2O_9$ and $Ca_3NiNb_2O_9$ with distorted structures, the easy-axis anisotropy is excluded by the LSW approximation of the INS measurements while two magnetic transitions are observed in both compounds. An extra noncollinear magnetic phase exists at low temperature, which corresponds to the phase transition at T_{N1}. For the $S = 1$ case, the high-temperature transition from the paramagnet is not clear and a different phase diagram has been proposed by the different theories; specifically the stripe phase is related to a spin reorientation in the honeycomb lattice [35], and the zigzagging stripe phase in the isosceles triangular networks by the harmonic particle interaction [36].

V. CONCLUSIONS

In summary, the lattice distortion effect on the magnetic ground states of spin-1 TLAFs was investigated by comparing two isosceles triangular lattice antiferromagnets $Sr_3NiNb_2O_9$ and $Ca_3NiNb_2O_9$ with an equilateral triangular compound $Ba_3NiNb_2O_9$. Although the effective magnetic moment across the family is the same, the magnetic frustration of the system increases from the equilateral triangle to the isosceles one. Moreover, the two magnetic phase transitions were observed in $A =$ Sr and Ca compared to one in $A =$ Ba. However, the lattice distortion did not tune the easy-plane anisotropy of the Ba compound. Instead, the lattice distortion generated an extra competitive magnetic phase with strip configuration at low temperatures for both Sr and Ca compounds and yielded larger interplane exchange energy with greater anisotropy for the ground state of the spin-1 $A_3NiNb_2O_9$ TLAF.

ACKNOWLEDGMENTS

J.M. and G.H.W. acknowledge support from National Science Foundation of China (Grant No. 11774223). We are thankful for support from NSF-DMR through Grant No. DMR-1350002. Research conducted at ORNL's High Flux Isotope Reactor was sponsored by the Scientific User Facilities Division, Office of Basic Energy Sciences, and U.S. Department of Energy. The work is supported by the Starting-up Fund of Shanghai Jiao Tong University (Shanghai, People's Republic of China) and Thousand-Youth-Talent Program of People's Republic of China.

[1] A. V. Chubokov and D. I. Golosov, J. Phys.: Condens. Matter **3**, 69 (1991).
[2] A. P. Ramirez, Annu. Rev. Mater. Res. **24**, 453 (1994).
[3] L. Balents, Nature (London) **464**, 199 (2010).
[4] T. Sakai and H. Nakano, Phys. Rev. B **83**, 100405 (2011).
[5] M. Mourigal, W. T. Fuhrman, A. L. Chernyshev, and M. E. Zhitomirsky, Phys. Rev. B **88**, 094407 (2013).
[6] J. Alicea, A. V. Chubukov, and O. A. Starykh, Phys. Rev. Lett. **102**, 137201 (2009).
[7] J. G. Cheng, G. Li, L. Balicas, J. S. Zhou, J. B. Goodenough, C. Xu, and H. D. Zhou, Phys. Rev. Lett. **107**, 197204 (2011).
[8] J. Reuther and R. Thomale, Phys. Rev. B **83**, 024402 (2011).
[9] Y. Shirata, H. Tanaka, T. Ono, A. Matsuo, K. Kindo, and H. Nakano, J. Phys. Soc. Jpn. **80**, 093702 (2011).
[10] J. Hwang, E. S. Choi, F. Ye, C. R. Dela Cruz, Y. Xin, H. D. Zhou, and P. Schlottmann, Phys. Rev. Lett. **109**, 257205 (2012).
[11] Y. Shirata, H. Tanaka, A. Matsuo, and K. Kindo, Phys. Rev. Lett. **108**, 057205 (2012).
[12] M. Lee, J. Hwang, E. S. Choi, J. Ma, C. R. Dela Cruz, M. Zhu, X. Ke, Z. L. Dun, and H. D. Zhou, Phys. Rev. B **89**, 104420 (2014).
[13] T. Susuki, N. Kurita, T. Tanaka, H. Nojiri, A. Matsuo, K. Kindo, and H. Tanaka, Phys. Rev. Lett. **110**, 267201 (2013).
[14] O. A. Starykh and L. Balents, Phys. Rev. B **89**, 104407 (2014).
[15] M. Mourigal, M. Enderle, B. Fak, R. K. Kremer, J. M. Law, A. Schneidewind, A. Hiess, and A. Prokofiev, Phys. Rev. Lett. **109**, 027203 (2012).
[16] T. Ono, H. Tanaka, H. Aruga Katori, F. Ishikawa, H. Mitamura, and T. Goto, Phys. Rev. B **67**, 104431 (2003).
[17] Y. Fujii, T. Nakamura, H. Kikuchi, M. Chiba, T. Goto, S. Matsubara, K. Kodama, and M. Takigawa, Phys. B (Amsterdam, Neth.) **346–347**, 45 (2004).
[18] T. Ono, H. Tanaka, O. Kolomiyets, H. Mitamura, T. Goto, K. Nakajima, A. Oosawa, Y. Koike, K. Kakurai, and J. Klenke, J. Phys.: Condens. Matter **16**, S773 (2004).
[19] M. A. Fayzullin, R. M. Eremina, M. V. Eremin, A. Dittl, N. van Well, F. Ritter, W. Assmus, J. Deisenhofer, H.-A. Krug von Nidda, and A. Loidl, Phys. Rev. B **88**, 174421 (2013).
[20] S. A. Zvyagin, D. Kamenskyi, M. Ozerov, J. Wosnitza, M. Ikeda, T. Fujita, M. Hagiwara, A. I. Smirnov, T. A. Soldatov, A. Ya. Shapiro, J. Krzystek, R. Hu, H. Ryu, C. Petrovic, and M. E. Zhitomirsky, Phys. Rev. Lett. **112**, 077206 (2014).
[21] M. Lee, E. S. Choi, J. Ma, R. Sinclair, C. R. Dela Cruz, and H. D. Zhou, J. Phys.: Condens. Matter **28**, 476004 (2016).
[22] H. J. Xiang, E. J. Kan, Y. Zhang, M. H. Whangbo, and X. G. Gong, Phys. Rev. Lett. **107**, 157202 (2011).
[23] J. Rodríguez-Carvajal, Phys. B (Amsterdam, Neth.) **192**, 55 (1993).
[24] M. Russina, G. Guenther, V. Grzimek, R. Gainov, M. Schlegel, L. Drescher, T. Kaulich, W. Graf, B. Urban, A. Daske, K. Grotjahn, R. Hellhammer, G. Buchert, H. Kutz, L. Rossa, O. Sauer, M. Fromme, D. Wallacher, K. Kiefer, B. Klemke, N. Grimm, S. Gerischer, N. Tsapatsaris, and K. Rolfs, Phys. B (Amsterdam, Neth.) (2017), doi:10.1016/j.physb.2017.12.026.
[25] D. I. Woodward and I. M. Reaney, Acta Cryst. B **61**, 387 (2005).
[26] J. B. Philipp, P. Majewski, L. Alff, A. Erb, R. Gross, T. Graf, M. S. Brandt, J. Simon, T. Walther, W. Mader, D. Topwal, and D. D. Sarma, Phys. Rev. B **68**, 144431 (2003).
[27] J. Ma, Y. Kamiya, Tao Hong, H. B. Cao, G. Ehlers, W. Tian, C. D. Batista, Z. L. Dun, H. D. Zhou, and M. Matsuda, Phys. Rev. Lett. **116**, 087201 (2016).

[28] M. Liu, H. Zhang, X. Huang, C. Ma, S. Dong, and J. M. Liu, Inorg. Chem. **55**, 2709 (2016).
[29] M. Lee, E. S. Choi, X. Huang, J. Ma, C. R. Dela Cruz, M. Matsuda, W. Tian, Z. L. Dun, S. Dong, and H. D. Zhou, Phys. Rev. B **90**, 224402 (2014).
[30] S. Toth, B. Lake, S. A. J. Kimber, O. Pieper, M. Reehuis, A. T. M. N. Islam, O. Zaharko, C. Ritter, A. H. Hill, H. Ryll, K. Kiefer, D. N. Argyriou, and A. J. Williams, Phys. Rev. B **84**, 054452 (2011).
[31] J. Kanamori, J. Phys. Chem. Solids **10**, 87 (1959).
[32] K. Yokota, N. Kurita, and H. Tanaka, Phys. Rev. B **90**, 014403 (2014).
[33] A. Möller, N. E. Amuneke, P. Daniel, B. Lorenz, C. R. dela Cruz, M. Gooch, and P. C. W. Chu, Phys. Rev. B **85**, 214422 (2012).
[34] R. Sinclair, H. D. Zhou, M. Lee, E. S. Lorenz, G. Li, T. Hong, and S. Calder, Phys. Rev. B **95**, 174410 (2017).
[35] J. Merino and A. Ralko, Phys. Rev. B **97**, 205112 (2018).
[36] F. Leoni and Y. Shokef, Entropy **20**, 122 (2018).